Long-term ionospheric anomaly monitoring for ground based augmentation systems

Sungwook Jung[1] and Jiyun Lee[1]

Received 18 March 2012; revised 28 May 2012; accepted 6 June 2012; published 25 July 2012.

[1] Extreme ionospheric anomalies can pose a potential integrity threat to ground-based augmentation of the Global Positioning System (GPS), and thus the development of ionospheric anomaly threat models for each region of operation is essential for system design and operation. This paper presents a methodology for automated long-term ionospheric anomaly monitoring, which will be used to build an ionospheric anomaly threat model, evaluate its validity over the life cycle of the system, continuously monitor ionospheric anomalies, and update the threat model if necessary. This procedure automatically processes GPS data collected from external networks and estimates ionospheric gradients at regular intervals. If ionospheric gradients large enough to be potentially hazardous to users are identified, manual data examination is triggered. This paper also develops a simplified truth processing method to create precise ionospheric delay estimates in near real-time, which is the key to automating the ionospheric monitoring procedure. The performance of the method is examined using data from the 20 November 2003 and 9 November 2004 ionospheric storms. These results demonstrate the effectiveness of simplified truth processing within long-term ionosphere monitoring. From the case studies, the automated procedure successfully identified extreme ionospheric anomalies, including the two worst ionospheric gradients observed and validated previously based on manual analysis. The automation of data processing enables us to analyze ionospheric data continuously going forward and to more accurately categorize ionospheric behavior under both nominal and anomalous conditions.

Citation: Jung, S., and J. Lee (2012), Long-term ionospheric anomaly monitoring for ground based augmentation systems, *Radio Sci.*, *47*, RS4006, doi:10.1029/2012RS005016.

1. Introduction

[2] The Local Area Augmentation System (LAAS), which is a form of Ground-Based Augmentation Systems (GBAS) developed by the U.S. Federal Aviation Administration (FAA), supports aircraft precision approach and landing in the Conterminous United States (CONUS). LAAS consists of the equipment and software necessary to augment the U.S. Department of Defense (DoD)-provided GPS Standard Positioning Service (SPS). The LAAS ground facility (LGF) is a reference station equipped with typically four GPS receivers and antennas sited at surveyed locations within the property of a particular airport, as illustrated in Figure 1. The GBAS reference station, such as the LGF, broadcasts differential GPS corrections and integrity information to aviation users within several tens of kilometers of GBAS-equipped airports via a VHF Data Broadcast (VDB) transmitter. GBAS users improve positioning accuracy by applying these corrections to their L1 measurements, thus eliminating common errors between users and the reference receivers. The integrity information allows the users within the specified GBAS service volume to eliminate any satellites impacted by any system failures from its position calculation and compute error bounds on its position solution with extremely high confidence and thus verify the safety of approach and landing operations in real time.

[3] The GBAS reference station monitors any system failures or threats which may pose integrity risks to users. One of the most challenging hazards to mitigate is the extremely large spatial decorrelation that can exist in the ionosphere during ionospheric storms. Ionospheric spatial gradients in the slant domain (i.e., along the actual path between satellite and receiver) as large as 412 mm/km at high elevation and 360 mm/km at low elevation [*Pullen et al.*, 2009; *Lee et al.*, 2011a] were observed in the United States during the geomagnetic storm of 20 November 2003. While differential GBAS user errors due to spatial variations in ionospheric delay are almost negligible under nominal conditions, GBAS reference stations and users may experience very different ionospheric delays under ionosphere storm conditions; thus residual ionospheric errors (after differential corrections are

[1]Korea Advanced Institute of Science and Technology, Daejeon, South Korea.

Corresponding author: J. Lee, Korea Advanced Institute of Science and Technology, 291 Daehak-ro, Daejeon 305-701, South Korea. (jiyunlee@kaist.ac.kr)

0048-6604/12/2012RS005016

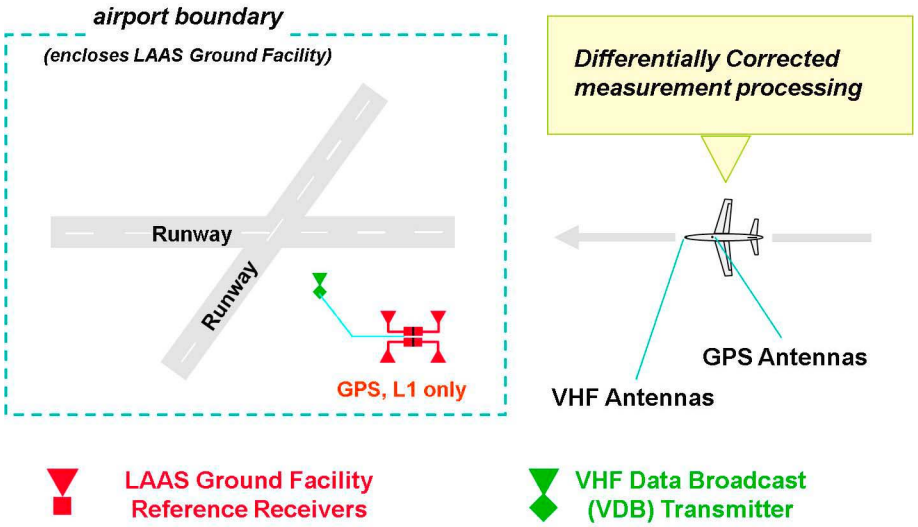

Figure 1. Illustration of a typical Local Area Augmentation System (LAAS) configuration.

applied) could be unacceptably large. For a GBAS user at a 200-foot decision height and 6 km from the reference station, a spatial gradient of 412 mm/km could cause a residual range error of 0.412 m/km × 20 km = 8.2 m. Here, the effective separation of 20 km results from the sum of the actual distance of 6 km between the reference station and the user and the 14 km of "synthetic separation" generated by the memory of the code-carrier smoothing filter [*Pullen et al.*, 2009]). If this large ionospheric spatial gradient is undetected by the reference station, the resulting range errors could produce vertical position errors for GBAS users of a few tens of meters when combined with the worst-case airborne satellite geometries and approach timing.

[4] To predict the maximum position errors that LAAS users might suffer from this threat, an ionospheric anomaly "threat model" for LAAS was generated for CONUS. A detailed manual data-analysis method was developed and used to examine past Global Positioning System (GPS) dual-frequency data collected from the network of Continuously Operating Reference Stations (CORS) and Wide Area Augmentation System (WAAS) reference stations [*Ene et al.*, 2005; *Datta-Barua et al.*, 2010]. The threat model derived from this data analysis is used to simulate worst-case ionospheric errors and, by processing through a model of GBAS behavior during these events [*Lee et al.*, 2011b], worst-case GBAS user position errors in the presence of ionospheric anomalies. These hypothetical errors can be mitigated to acceptable levels by inflating one or more broadcast integrity parameters in near real time [*Lee et al.*, 2011b]. A targeted inflation method has recently been developed to mitigate this threat while reducing the resulting loss of availability by inflating satellite-specific broadcast parameters [*Seo et al.*, 2012].

[5] An anomalous ionospheric spatial gradient is modeled as a spatially linear semi-infinite wedge (parameterized by the gradient or "slope" of the ramp and its width) or "front" moving with constant speed, as shown in Figure 2. The upper bounds of these parameters were determined through a comprehensive search of days with severe ionospheric behavior which took several years [*Datta-Barua et al.*, 2010]. The current set of bounding parameter values that form the ionospheric anomaly threat model for LAAS Category (CAT) I precision approaches [*Radio Technical Commission for Aeronautics* (*RTCA*), 2004] in CONUS is summarized in Table 1. The upper bound on the gradient is given as a function of satellite elevation angle: 375 mm/km at low elevation (below 15 degrees), increasing linearly to 425 mm/km at high elevation (above 65 degrees). These bounds slightly exceed the largest gradient observed from the CONUS data analysis due to margin added to account for measurement and estimation errors. Maximum bounds or ranges were also established on ionospheric front speed with respect to the ground (up to 750 m/s), ionospheric front width (between 25 to 200 km), and total differential delay (up to 50 m). This model was used for safety assessment and System Design Approval (SDA) of the Honeywell SLS-4000 LAAS Ground Facility (LGF) for use in CONUS (J. Warburton, Ionosphere

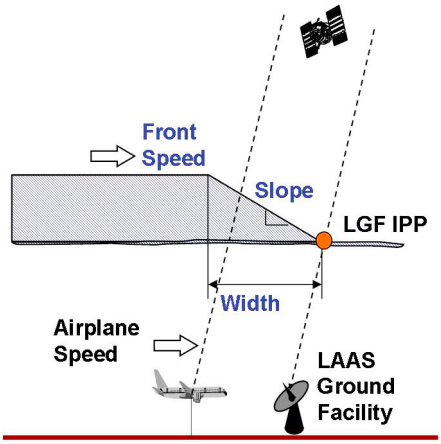

Figure 2. Illustration of a LAAS user impacted by an ionospheric wavefront (modeled as a linear semi-infinite wedge with the slope of the ramp, its width, and a constant propagation speed).

Table 1. Ionospheric Anomaly Threat Model for LAAS Category (CAT) I Precision Approach

Parameters	Bounds or Ranges of Parameters	
Max. Front slope (mm/km)	Low elevation (<15°)	375
	Medium elevation (15° < el < 65°)	375 + 50(el-15)/50
	High elevation (>65°)	425
Front width (km)	25–200	
Front speed (m/s)	0–750	
Max. differential delay (m)	50	

threat update, submitted to the International GBAS Working Group, 2008).

[6] However, even within CONUS, the SLS-4000 threat model has limitations because it is based upon on a small number of severe ionospheric events whose probability cannot easily be determined. In addition, the station separations within the CORS network (typically 40–100 km) do not reflect the GBAS architecture, given that the distance between the GBAS reference station and users at the CAT I decision height (DH) is no more than 5–10 km. Because of these limitations, it is not acceptable to rely upon the existing threat model indefinitely without further investigation. Therefore, ionospheric anomalies will be monitored over the life cycle of GBAS, and the threat model will be updated if necessary.

[7] An automated procedure for long-term ionospheric anomaly monitoring is required to continually monitor ionospheric behavior as long as GBAS is dependent on the outer bounds of ionospheric threat models. This paper presents a methodology to process GPS data automatically at regular intervals and trigger manual data examination if gradients large enough to potentially threaten GBAS users are discovered. The validation procedures are automated as much as possible. However, resources for manual validation must be retained because automated results cannot be trusted by themselves. Section 2 provides an overview of the Long-term Ionospheric Anomaly (LTIA) monitor. Section 3 explains the data input to the LTIA monitor, Section 4 describes the monitor algorithm procedures in detail, and Section 5 presents the outputs of the monitor. In Section 6, the performance of the monitor is evaluated by conducting case studies on both nominal and storm days. Section 7 presents our concluding remarks.

2. Overview of Long-term Ionospheric Anomaly (LTIA) Monitor

[8] The methodology for long-term ionospheric observation and anomaly monitoring has been developed based on the data analysis and verification techniques used to generate the CONUS ionospheric threat model [*Datta-Barua et al.*, 2010]. This procedure is composed of three steps, as shown in Figure 3: Data Collection Processing (DCP), Ionospheric Anomaly Search Processing (IASP), and Reporting. Most of the LTIA steps are automated procedures, except the last step of Ionospheric Anomaly Search Processing (Manual Validation that requires personal intervention) and Reporting.

[9] The LTIA monitor begins with gathering GPS data and external information from public space weather sites. This external data is used to select potential periods of anomalous ionospheric events in the Ionospheric Anomaly Search Processing (IASP). This processor consists of four functions: Ionospheric Event Search (IES), Ionospheric Delay and Gradient Estimation (IDGE), Ionospheric Anomaly Candidate Screening (IACS), and Manual Validation (MV). IES selects periods of interest based on the data collected from external sources. IDGE chooses and processes data of subsets of CORS stations with short separations (e.g., less than 100 km) and computes ionospheric gradients between stations. This is done by creating "simple Truth" data (meaning precise ionospheric delay measurements using an automated procedure instead of the off-line post-processing approach described in [*Komjathy et al.*, 2004, 2005]) using

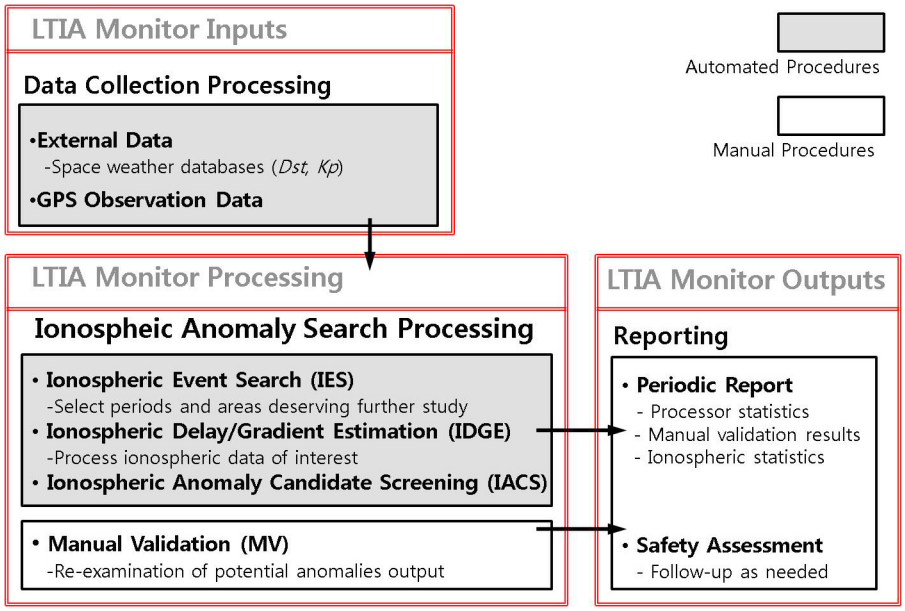

Figure 3. Methodology of long-term ionospheric anomaly monitoring.

dual-frequency CORS data. IACS is designed to automatically search for any anomalous gradients which exceed a threshold and also pass automated "false-alarm" screening. The selected anomaly candidates will be manually validated at the last step of IASP. If an anomalous event is validated by manual analysis, it will be included in a periodic report. The details of each step are described in Section 4.

[10] The LTIA monitor is designed to mainly detect anomalously large gradients (i.e., the slope of the linear ramp), which is the most critical parameter to the impact on single-frequency GBAS users. The impact of ionospheric wavefronts on GBAS is not very sensitive to width, and thus the automated algorithm does not attempt to estimate of the width of wavefront. The impact on GBAS users is maximized when the Ionospheric Pierce Point (IPP) of the GBAS reference station moves with approximately the same speed and direction of the ionospheric wavefront, as this makes the resulting gradients undetectable to the reference station [*Pullen et al.*, 2009]. Because the existing range of ionospheric front speeds already includes this worst-case condition, front speed with respect to the ground is not a parameter which may result in a major change in the GBAS impact assessment.

3. LTIA Monitor Inputs

3.1. GPS Observation Data

[11] The Long-term Ionospheric Anomaly (LTIA) monitor processes GPS observation data collected from the CORS network (possibly supplemented by data from new stations in the future) automatically at regular intervals and triggers manual data examination if ionospheric gradients large enough to potentially threaten GBAS users are discovered. The GPS data of CORS stations can be obtained from the CORS network FTP service (ftp://www.ngdc.noaa.gov/cors) which allows access to anonymous users. The service provides GPS observation data, navigation data of GPS satellites, and coordinates of CORS stations. The details of this service are from the National Geodesy Survey (NGS) in the U.S. National Oceanic and Atmospheric Administration (http://www.ngs.noaa.gov/CORS).

[12] The general form of the GPS code (ρ_1, ρ_2) and carrier-phase (ϕ_1, ϕ_2) observables for the L1 and L2 signal frequencies are expressed as

$$\begin{aligned}
\rho_{L1} &= r_i^k + I_i^k + \varepsilon_{\rho_1} \\
\phi_{L1} &= r_i^k - I_i^k + N_{L1} + \varepsilon_{\phi_1} \\
\rho_{L2} &= r_i^k + \gamma I_i^k + c\left(IFB_i + \tau_{gd}^k\right) + \varepsilon_{\rho_2} \\
\phi_{L2} &= r_i^k - \gamma I_i^k - c\left(IFB_i + \tau_{gd}^k\right) + N_{L2} + \varepsilon_{\phi_2} \\
\gamma &= \frac{f_{L1}^2}{f_{L2}^2}
\end{aligned} \tag{1}$$

[13] The common term, r, represents the sum of the true range between the ith receiver and kth satellite, receiver/satellite clock biases and tropospheric error. The carrier phase observables contain an integer ambiguity, N, but have lower multipath and thermal noise errors than the code measurements (i.e., $\varepsilon_\phi \ll \varepsilon_\rho$). The ionospheric error, I, is of equal magnitude but opposite sign on the carrier phase relative to the code phase. The ionospheric delay at the L2 frequency (f_{L2}) is proportional to the delay I at the L1 frequency (f_{L1}) by the squared frequency ratio γ. By taking the advantage of this dispersive nature of the ionosphere, ionospheric delays can be computed from the dual-frequency observables. The hardware differences in the L1 and L2 signal paths cause inter-frequency biases on both receiver (IFB) and satellite (τ_{gd}). The parameter c is the speed of light in vacuum.

[14] The slant ionospheric delay on the L1 signal is calculated using the L1/L2 code and carrier measurements, as shown in equation (2). The primary difficulty of ionospheric delay computation with dual-frequency GPS data is to deal with main error sources: inter-frequency hardware biases on the receiver, *IFB*, and satellite, τ_{gd}. The method of IFB calibration will be discussed in Section 4.2.2.

$$\begin{aligned}
I_{\rho_i}^k &= \frac{\rho_{L2} - \rho_{L1}}{\gamma - 1} = I + \frac{c}{\gamma - 1}\left(IFB_i + \tau_{gd}^k\right) + \varepsilon_\rho \\
I_{\phi_i}^k &= \frac{\phi_{L1} - \phi_{L2}}{\gamma - 1} = I + \frac{c}{\gamma - 1}\left(IFB_i + \tau_{gd}^k\right) + \frac{N_{L1} - N_{L2}}{\gamma - 1} + \varepsilon_\phi
\end{aligned} \tag{2}$$

[15] The dual-frequency code-derived estimate I_ρ is noisier than the carrier-derived estimate I_ϕ because the carrier phase measurements have lower multipath and thermal noise errors than the code measurements (i.e., $\varepsilon_\phi \ll \varepsilon_\rho$). Thus, I_ϕ is used to obtain precise estimates of ionospheric delays in this study. The integer ambiguities, N_{L1} and N_{L2}, are removed by fitting I_ϕ to I_ρ (see Section 4.2.1).

3.2. Space Weather Data

[16] The automated tool first gathers external information from public space weather sites at regular intervals. This external data is used to select potential periods of anomalous ionospheric events in Ionospheric Event Search (IES) (which will be described in Section 4.1). In Data Collection Processing (DCP), the LTIA monitor collects two indices of global geomagnetic activity from space weather databases: planetary K (Kp) and *disturbance, storm time* (Dst). Kp represents solar particle effects on the Earth's magnetic fields, and is a three-hour composite index measured at several midlatitude stations primarily located in the northern hemisphere [*Menvielle and Berthelier*, 1991]. The Kp index ranges from 0 (no activity) to 9 (extreme activity) in thirds of an index unit. The Dst index measures equatorial magnetic disturbance derived from hourly scaling of low-latitude horizontal magnetic variation [*Sugiura and Kamei*, 1991]. A negative Dst with a higher magnitude indicates that a more intense magnetic storm is in progress.

[17] To operate this monitoring system on a daily basis (as a default), it requires external data with a data rate of at least once per day. The Kp and Dst indices are available from the National Oceanic and Atmospheric Administration (NOAA). NOAA provides two types of data for the Kp index: the estimated and final values. The final value provided by the National Geophysical Data Center (NGDC) of NOAA (ftp://ftp.ngdc.noaa.gov) is not adequate for this monitoring system because of a low data rate (updated on a monthly basis). The LTIA monitor instead uses the estimated value of Kp provided by the Space Weather Prediction Center (SWPC) of NOAA (ftp://ftp.swpc.noaa.gov) with an

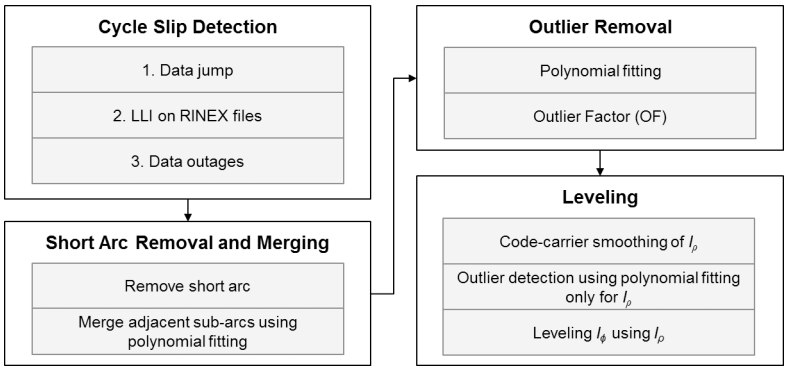

Figure 4. Algorithm for generating "simple Truth" data.

update rate of every three hours. NGDC also provides three types of Dst: the final, preliminary, and real-time values. However, the latency of data is approximately a month at shortest. Thus, this monitor collects the real-time Dst from an alternative source, the World Data Center for Geomagnetism at Kyoto University (http://wdc.kugi.kyoto-u.ac.jp). Their data (known as "Quick-look") are updated every hour.

4. LTIA Monitor Processing

[18] The core of the LTIA monitor is Ionospheric Anomaly Search Processing (IASP) which consists of Ionospheric Event Search (IES), Ionospheric Delay and Gradient Estimation (IDGE), Ionospheric Anomaly Candidate Screening (IACS), and Manual Validation (MV).

4.1. Ionospheric Event Search (IES)

[19] The LTIA monitor processes the external data on a daily basis (as a default) and flags potential periods of severe ionospheric storm conditions for further automated analysis.

[20] A particular day is selected if the daily maximum value of Kp is greater than six and that of Dst is less than −200. These selection criteria were pre-determined carefully to satisfy the requirement of discriminating all potential storm periods conservatively while minimizing false detection. If these criteria are applied to the data from 2000 to 2004 which includes the last solar maximum period, all dates from which data have been analyzed to build the current CAT I threat model (listed in Table 1 of [*Datta-Barua et al.*, 2010]) are selected except two dates, 7 Sept. 2002 and 17 July 2004. However, from the fact that no threat points within the threat model have been derived from those two dates, it is confirmed that the selection thresholds are well determined. Note that while the level of ionospheric disturbance often correlates closely with the level of geomagnetic disturbance, there could be exceptional cases. Thus the most conservative approach to capture the entire range of abnormal ionospheric behavior is to run the monitor daily regardless of Kp and Dst indices.

4.2. Ionospheric Delay and Gradient Estimation (IDGE)

[21] High-quality ionospheric measurements are essential for the long-term ionospheric anomaly monitoring. Precise estimates of ionospheric delays can be obtained using dual-frequency GPS data from networks of stations and sophisticated post-processing algorithms. The current ionospheric threat model for LAAS was built using ionospheric delay estimates produced by the Jet Propulsion Laboratory (JPL). They collected data from the CORS and WAAS network stations and post-processed those in the "Supertruth" processing described by [*Komjathy et al.*, 2004, 2005]. The LTIA monitor requires automatically and independently generating ionospheric estimates which are comparable to the "Supertruth" solution in terms of accuracy. A new method of generating "simple Truth" data which is simpler and faster than "Supertruth" processing was developed in this study. Figure 4 shows the procedures of the truth processing. The dual-frequency GPS data, which are automatically collected from the CORS network, are inputs to generate precise ionospheric delay estimates. The truth processing detects obvious cycle slips of raw data, levels carrier-phase measurements using code measurements, and estimates satellite/receiver inter-frequency biases (IFB). This section explains the method of generating "simple Truth" data, which is simpler and faster than "Supertruth" processing, and the method of estimating ionospheric gradients using the "simple Truth" solutions.

4.2.1. Pre-processing

[22] This section describes pre-processing of the slant ionospheric delays on the L1 frequency computed from the L1/L2 code and carrier measurements: the code-derived, I_ρ, and carrier-derived, I_ϕ., estimates shown in equation (2). The pre-processing of these measurements includes cycle slip detection, short arc removal, outlier removal, and code-carrier smoothing, as shown in Figure 5. Cycle slip detection is performed for each continuous arc of I_ϕ., which is at least 3600 s (as default) apart from adjacent arcs. Arcs with the time separation shorter than 3600 s are identified through the cycle slip detection process. Three detection criteria are applied to identify cycle slips of carrier-derived observables. First, a difference between two adjacent data points is examined to detect a large jump greater than a slip detection parameter (2.5 m for a storm day and 0.8 m for a nominal day). Second, the Loss of Lock Indicator (LLI) of each observation from raw GPS data in RINEX format is utilized as an indicator of potential cycle slips. Third, the absence of L1 or L2 carrier measurements is also considered as potential cycle slips.

[23] Short arcs need to be discarded because leveling errors of those arcs are typically large and thus make delay

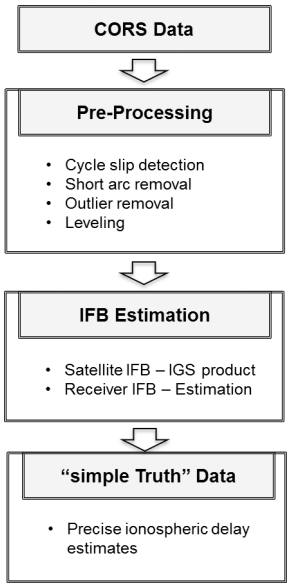

Figure 5. Preprocessing procedure of the LTIA monitor.

estimates useless. Data arcs which contain less than ten data points or five minutes in duration are removed from further consideration. Continuous arcs are divided into several sub-arcs after the cycle slip detection and the short arc removal. Furthermore, some outliers are flagged by the first criterion of the cycle slip detection process and misinterpreted as cycle slips. Consequently the outliers divide a continuous arc into several fragments. The polynomial fit method is utilized to merge two successive sub-arcs, misleadingly divided by an outlier, into one continuous arc. The residual, the I_ϕ. data minus the polynomial fit, at the last point of the first arc and the residual at the first point of the second arc are compared. If these differential residuals between sub-arcs are less than 0.8 m, those are considered as a continuous arc.

[24] After performing detection of cycle slips, the steps of outlier detection and removal are carried out for each continuous arc. Two approaches, the polynomial fit method and the adjacent point difference method, are executed in parallel. First, a polynomial fit, P_{fit}, is performed on the carrier-derived observables, I_ϕ. The residuals (i.e., the I_ϕ. data minus the polynomial fit), R, and the differential residuals,∇ R, of the fit are computed for each epoch, t, as shown in equation (3).

$$\begin{aligned} R(t) &= I_\phi(t) - P_{fit}(t) \\ \nabla R(t) &= R(t) - R(t-1) \\ \nabla R(t_{\max}) &= \max_t(\nabla R) \end{aligned} \tag{3}$$

[25] Note that this polynomial fit is performed independently from the polynomial fit method previously used to combine sub-arcs. If the largest jump, $\nabla R(t_{\max})$, between adjacent points exceeds an outlier detection parameter of 0.8 m, the point, $I_\phi(t_{\max})$, is classified as a potential outlier. Second, the difference between adjacent points is computed using the adjacent point difference algorithm in [Kou *et al.* 2006]. The averaged difference, Outlier Factor (*OF*), between adjacent points of the point p at time t_p is calculated by equation (4).

$$\begin{aligned} OF(t_p) &= \sum_{q \in Adjacent} w_{pq} \cdot |I_p - I_q| \\ w_{pq} &= \frac{1/|t_p - t_q|}{\sum_{r \in Adjacent} 1/|t_p - t_r|} \\ OF(t_{p\_\max}) &= \max_{t_p}(OF) \end{aligned} \tag{4}$$

[26] The set "*Adjacent*" includes all points within fifteen minutes centered at the point *p*. *w* is the weight between two points, *p* and *q*. If the outlier candidate identified from the polynomial fit method returns the largest *OF*, (i.e., if $t_{\max} = t_{p\_\max}$) the point is confirmed as an outlier. This process is repeated until no more outlier remains.

[27] Next, a 150 s carrier-smoothing window to smooth the 30-s code-derived observables, I_ρ, is applied to mitigate multipath errors on the code measurements. Prior to the smoothing process, the outliers of I_ρ are detected and removed using only the polynomial fit method with a detection threshold of 10 m. The smoothed code measurements are used to level the carrier-derived measurements. The carrier-derived observable, I_ϕ, contains integer ambiguities from both L1 and L2 frequencies. To remove these ambiguities, I_ϕ is fitted to I_ρ, introducing a level parameter, L [*Komjathy et al.*, 2004].

$$L = \frac{\sum_{i=1}^{N} \left(I_\rho(t_i) - I_\phi(t_i)\right) \sin^2 el_i}{\sum_{i=1}^{N} \sin^2 el_i} \tag{5}$$

[28] The level is computed for each continuous arc by averaging the difference between I_ρ and I_ϕ over the epoch t_i (i = 1, 2, …, N) using an elevation (*el*)-dependent weighting. To mitigate the multipath effects further, data with elevation angles less than 10 degrees are discarded. The leveled carrier-derived estimates, $I_{\phi\_leveled}$, can be written as

$$I_{\phi\_leveled} = I_\phi + L = I + \frac{c}{\gamma - 1}\left(IFB + \tau_{gd}\right) \tag{6}$$

[29] In equation (6), the receiver and satellite hardware biases (*IFB* and τ_{gd}) must be removed to obtain ionospheric delay estimates, I. The parameter γ is the squared L1/L2 frequency ratio and c is the speed of light in a vacuum.

4.2.2. IFB Estimation

[30] The estimation technique of the inter-frequency biases was studied by many researchers [*Komjathy et al.*, 2004; *Ma and Maruyama*, 2003]. The well-known methods assume a mathematical function to model the variation of ionospheric delays, and estimate the coefficients of the model and IFB simultaneously using a Kalman filter. These approaches were proven to estimate ionospheric delays with a high accuracy, but do not support long-term ionospheric anomaly monitoring for GBAS due to an extensive amount of processing time. The LTIA monitor implements a simpler and faster method to estimate a single receiver IFB, given by

Ma and Maruyama [2003]. The method utilizes the satellite hardware biases already determined from other parties.

[31] Several sources of the GPS satellite hardware bias, τ_{gd}, are available including the International GNSS Service (IGS) and the Centre for Orbit Determination in Europe (CODE) at the University of Berne. This automated tool uses satellite biases provided by the IGS central bureau (http://igscb.jpl.nasa.gov). The IGS product can be obtained from four Global Data Centers (GDCs) [*Hernández-Pajares et al.*, 2009].

[32] The underlying assumption for the receiver IFB estimation is that the variation of vertical ionospheric delays from all visible satellites at a given instant becomes minimal when the IFBs are correctly removed. The leveled carrier-derived estimates, $I_{\phi\_leveled}$, from equation (6) are converted to equivalent vertical delays via a geometric mapping function [*Datta-Barua et al.*, 2010], and used as inputs to a search algorithm. The best estimate of each receiver IFB is determined by searching for the one which minimizes the cumulative standard deviation of vertical ionospheric delays to their mean on a given day. An elevation cut-off angle of 30 degrees was applied for this algorithm to improve estimation accuracy.

[33] After removing both receiver and satellite hardware biases from $I_{\phi\_leveled}$, the LTIA Monitor obtain precise ionospheric delay estimates (i.e., "simple Truth" data). Using this "simple Truth" solution and the well-known "station pair method" [*Lee et al.*, 2007], the monitor computes ionospheric gradients from all possible pairs of selected CORS stations looking at each satellite. The pairs of stations are considered as though they represent an LGF-user receiver pair. The slant spatial gradient of ionospheric delay, ∇I, is estimated by dividing the difference in slant ionospheric delay between two stations i and j viewing the same satellite k by the baseline distance, d, between two stations at each epoch t.

$$\nabla I(t) = \frac{I_i^k(t) - I_j^k(t)}{d} \tag{7}$$

[34] Stations and times with apparently severe spatial gradients are output to automated screening algorithms that attempt to remove receiver glitches or post-processing errors from consideration.

4.3. Ionospheric Anomaly Candidate Screening (IACS)

[35] An automated process searches for any severe ionospheric gradients, ∇I, which exceeds a threshold (currently 300 mm/km in slant domain). Because a considerably large number of these gradients is not due to ionospheric events, any faulty candidates of ionospheric anomalies are discarded via a series of automated screening algorithms: the negative delay check, the excessive-bias check, and the L1 code-carrier check.

[36] Cases for which ionospheric delay estimates from one receiver have negative values or do not vary over time are attributed to a faulty receiver. These cases often exhibit a large bias on delay estimates resulting in misleading large gradients. First, the negative delay check eliminates candidates which show the negative values of delay estimates. During extreme ionospheric activities, erratic variations of gradients in time are typically observed. Thus, ionospheric gradients which are extremely large but steady over time are most likely false candidates. These cases can be removed by the excessive-bias check. It computes the mean of ionospheric gradients of a sub-arc where an anomaly candidate is identified. If the differences between gradients and the mean of the gradients are less than a threshold of 50 mm/km over the entire (i.e., 100%) sub-arc, the candidate is discarded in this process.

[37] The L1 code-carrier check, the final step of IACS, automates a part of process which has been originally performed by manual validation. If a L1 code-minus-carrier measurement is not available at a given epoch where an extreme gradient is observed, the candidate is discarded because manual validation (which is explained in Subsection 4.4) cannot be performed. At the next step of the L1 code-carrier check, the dual-frequency estimates are compared with the L1 code-minus-carrier estimates. A large discrepancy between the dual-frequency derived and the L1-only derived estimates indicates that those estimates are corrupted by receiver faults or post-processing errors. The L1 code-carrier check is performed to the estimates which are within ± 1.5 h from the epoch of the candidate. If the number of data points for which the difference between two gradients exceeds a threshold (currently 150 mm/km) is greater than five (which also can be adjusted), the candidate is eliminated.

4.4. Manual Validation (MV)

[38] Once the automated procedure has isolated an apparently anomalous set of data, manual inspection is required to validate that the observed events are actually due to the ionosphere and not CORS receiver faults or data errors. While approaches to manual validation will vary based on the details of the automated outputs, the typical method is to re-examine the L1/L2 dual-frequency estimates visually to determine whether the resulting gradients look "reasonably" like ionospheric events [*Lee et al.*, 2011a]. This process was automated to the extent possible as explained in Subsection 4.3. However, some degrees of personal intervention are not avoidable because too many various and unique cases exist. Dual-frequency data are prone to semi-codeless tracking errors on L2 measurements, particularly for satellites at low elevation angles which have weaker received signal strengths. The dual-frequency estimates are compared with the raw measurements derived from the L1 frequency code-carrier divergence. This L1-only measurement is more robust to outages and cycle slips. If both the dual-frequency and single-frequency estimates are in a good agreement, the gradient is declared to be "Validated."

5. LTIA Monitor Outputs

[39] If an anomalous event is substantially validated by manual analysis, it will be reported periodically along with processor and ionospheric gradient statistics. It is expected that commonly nothing requiring manual validation is found in a given time period. In that case, ionospheric statistics from automated procedures will be supplied in periodic reports. The reports will occasionally be filled with manual validation results in addition to automated results statistics. These results would be reviewed and, if they exceed the

Table 2. Dates and Conditions Analyzed for Case Studies

	Day (UT mm/dd/yy)	
	11/20/03	11/09/04
K_p	8.7	8.7
D_{st}	−472	−223
Geomagnetic Storm class	Extreme	Severe

bounds of the current threat model, a change to that model would be considered. Note that the periodic reports will be produced manually.

6. Monitoring Results

[40] To examine the performance of the automated component of long-term ionospheric anomaly monitoring, case studies were conducted on both nominal and ionospheric storm days. The dates from which data were collected and analyzed are shown in Table 2. On 20 November 2003, the effects of an earlier coronal mass ejection (CME) from the Sun triggered one of the most severe geomagnetic storms of the past solar cycle. This led to the most extreme ionospheric gradients observed to date in CONUS [*Pullen et al.*, 2009; *Lee et al.*, 2011a]. Thus, the first test was conducted on the 20 November 2003 ionospheric storm to compare the automated results to those generated previously by offline manual analysis and confirm that the monitor successfully identifies the largest gradients. The second test was performed to see if the monitor produces incorrect anomaly candidates on nominal days. An ionospherically active - but not classified as "storm" - day is preferable for the purpose of this study. Thus, 9 November 2004, on which the geomagnetic storm class was 'severe,' was chosen among the data set (Table 1 from *Lee et al.* [2007]) previously analyzed to access nominal ionosphere decorrelation. Early work demonstrated that the ionospheric activity on this date did not produce any ionospheric spatial gradients greater than 25 mm/km [*Lee et al.*, 2007]. Anomalies smaller than this magnitude are not a threat to GBAS users [*Pullen et al.*, 2009]; thus this date can be classified as a "nominal" day. The results from these two case studies are summarized in Table 3, and details are in the following subsections.

6.1. Case Study on Ionospheric Storm Day

[41] On 20 November 2003, both of the space weather indices, Kp of 8.7 and Dst of −472 (see Table 2), exceed the selection criteria of 6 and −200, respectively. If this event occurred in the future, it would automatically be selected at the step of Ionospheric Event Search (IES) for further analysis. As of November 2003, the total number of CORS stations in CONUS was 368. The automated tool searches for stations which have nearby stations within 100 km, and the number of such stations is 278. The GPS dual-frequency data of these stations were automatically downloaded from the CORS ftp server. In Ionospheric Delay and Gradient Estimation (IDGE), the data were processed to obtain ionospheric delay and gradient estimates for all possible pairs of stations, considering all satellites in view. Next, Ionospheric Anomaly Candidate Screening (IACS) searched for any anomalous gradients greater than 300 mm/km and returned 57 candidates. Among those, 32 candidates, possibly caused by receiver measurement errors or post-processing errors, were removed by the automated false-alarm screening. Note that the automated screening is not faultless – some false events pass through it. Thus, we performed manual validation on the remaining 25 candidates, and sixteen candidates were finally confirmed to be actual ionospheric anomalies.

[42] The sixteen anomalies observed from this test are listed in Table 4 along with the gradient magnitude, baseline length, time of observation, impacted satellite, station pairs, satellite elevation angle, and station locations. The points that were identified in the dual-frequency data and subsequently validated with single-frequency L1 code-minus-carrier data are classified as "DF." The final values of gradients for the "DF" type were determined based on the dual-frequency estimates. The points that were validated by comparing the patterns of the dual-frequency estimates and the L1-only estimates but whose two gradient estimates exhibit considerably large differences are shown in "L1." For the "L1" type, the final estimates were derived from the L1 data. The events numbered 1, 5, and 10 in Table 4 are anomalies discovered in prior work and are included in the current threat model [*Datta-Barua et al.*, 2010]. Note that event numbers 1 and 5 are the worst spatial gradients at high (greater than 65 degrees) and low (lower than 15 degrees) elevation, respectively [*Pullen et al.*, 2009]. The other thirteen gradients are newly observed from this study. Unlike previous manual analysis, the automated procedures examine all possible station pairs; thus the LTIA monitor identified more threat points than those discovered previously.

[43] Note that, for the case of the worst gradient at high elevation (event number 1 in Table 4), the magnitude of the slope estimated is 386.8 mm/km, whereas the gradient

Table 3. Summary of Long-Term Ionospheric Anomaly Monitoring Results From Two Case Studies on an Ionospheric Storm Day (20 November 2003) and a Nominal Day (9 November 2004)

		20 Nov 2003	09 Nov 2004
Total Number of CORS Receivers in CONUS		368	508
Number of Stations with Baseline ≤100 km		278	391
Ionospheric Anomaly Candidate Screening (Ionospheric Gradients >300 mm/km, Satellite – Station Pair)		57	33
Automated False-Alarm Screening	Removed from Negative Delay Check	2	15
	Removed from Excessive Bias Check	24	17
	Removed from L1 CMC Check	6	1
Final Ionospheric Anomaly Candidates (Satellite – Station Pair)		25	0
Manually Validated Ionospheric Anomalies (Satellite – Station Pair)		16	0

Table 4. Summary of Manually Validated Ionospheric Anomalies Observed on 20 November 2003 in CONUS

	Station	Latitude (degree)	Longitude (degree)	Baseline (km)	PRN	Time (UT)	Gradient (mm/km)	Elevation (degree)	Type
1	GARF	41.4	−81.6	51.2	8	20:59:30	386.8	68.45	DF
	ZOB1	41.3	−82.2						
2	ERLA	39.0	−84.6	53.1	28	21:09:30	371.6	57.84	DF
	LEBA	39.4	−84.3						
3	COLB	40.0	−83.0	65.4	28	21:02:00	371.5	54.80	DF
	MTVR	40.4	−82.5						
4	KNTN	40.6	−83.6	59.1	28	21:05:30	367.0	57.13	DF
	SIDN	40.3	−84.2						
5	GARF	41.4	−81.6	74.5	26	21:17:00	351.7	11.43	DF
	WOOS	40.8	−82.0						
6	FREO	40.2	−81.3	73.6	26	21:16:00	335.7	10.61	DF
	LSBN	40.8	−80.8						
7	GODE	39.0	−76.8	23.7	8	20:56:00	327.5	67.02	DF
	USNO	38.9	−77.1						
8	ERLA	39.0	−84.6	65.6	28	21:09:30	315.4	57.44	DF
	GRTN	38.9	−83.9						
9	PKTN	39.0	−83.0	85.2	28	21:04:00	313.7	54.54	DF
	STKR	39.3	−82.1						
10	KNTN	40.6	−83.6	59.1	26	20:51:30	309.1	12.68	L1
	SIDN	40.3	−84.2						
11	MTVR	40.4	−82.5	65.5	28	21:00:30	307.1	54.20	DF
	WOOS	40.8	−82.0						
12	GRTN	38.9	−83.9	76.9	28	21:08:00	305.3	56.21	DF
	PKTN	39.0	−83.0						
13	GARF	41.4	−81.6	51.2	27	21:02:00	301.4	42.18	L1
	ZOB1	41.3	−82.2						
14	CASS	43.6	−83.2	49.8	28	20:24:00	230.5	43.25	L1
	HBCH	43.8	−82.6						
15	COLB	40.0	−83.0	65.4	26	21:03:30	219.6	12.04	L1
	MTVR	40.4	−82.5						
16	COVX	36.9	−75.7	79.7	28	20:50:00	146.7	43.13	L1
	GLPT	37.2	−76.5						

previously estimated using the JPL post-processed CORS truth data (generated from the "Supertruth" processing) was 412 mm/km [1]. Thus, the difference of approximately 25 mm/km exists between the "simple Truth" and CORS truth estimates. This discrepancy is mainly caused by IFB calibration errors. Figure 6 shows the CORS receiver IFB estimation results on 20 November 2003. The IFB estimates obtained from "simple Truth" processing, $IFB_{\_(simple\ truth)}$, are compared to the JPL post-processed CORS receiver biases, $IFB_{\_(CORS\ truth)}$. In order to directly compare the receiver IFB estimation results to the JPL CORS truth solutions, GPS satellite hardware biases estimated by the JPL "Supertruth" processing were used in the LTIA monitor processing for this test run. The mean difference between the two solutions is −1.227 ns, and the root-mean square (RMS) error is 1.711 ns. The percentage of stations whose errors are within ±2 ns is 74.4. Thus, the $IFB_{\_(simple\ truth)}$ and $IFB_{\_(CORS\ truth)}$ are in good agreement for a majority of stations.

[44] This demonstrates that the "simple Truth" method does a good job of estimating the receiver biases, considering that the poor performance of bias estimation is expected when ionospheric activity is severe [*Ma and Maruyama*, 2003], and the quality of JPL post-processed CORS data on storm days is also expected to be worse than that of nominal days. The IFB calibration error of 2 ns corresponds to approximately 0.93 m on L1 frequency measurement. Figure 7 compares slant ionospheric delay estimates from two solutions, "simple Truth" and "Supertruth." The top plot shows slant ionospheric delays observed between ZOB1 and

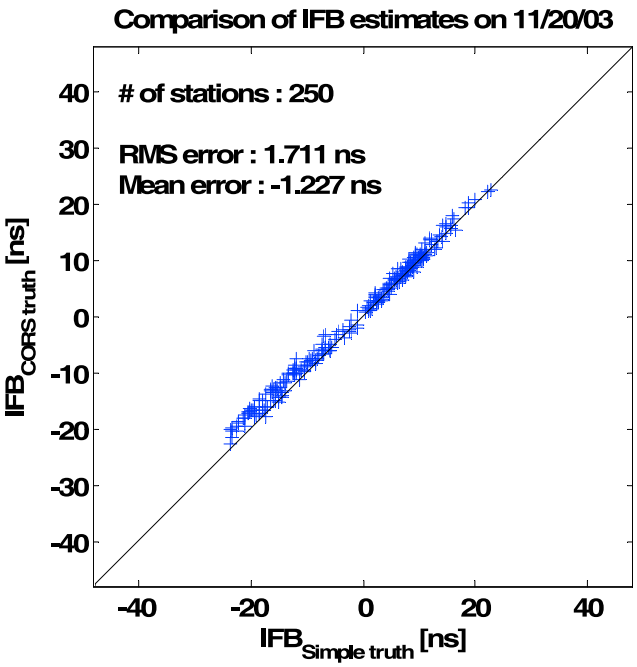

Figure 6. Comparison of CORS receiver IFB estimates on 20 November 2003. "Simple Truth" receiver biases, $IFB_{\_(simple\ truth)}$, are compared to JPL post-processed CORS receiver biases, $IFB_{\_(CORS\ truth)}$.

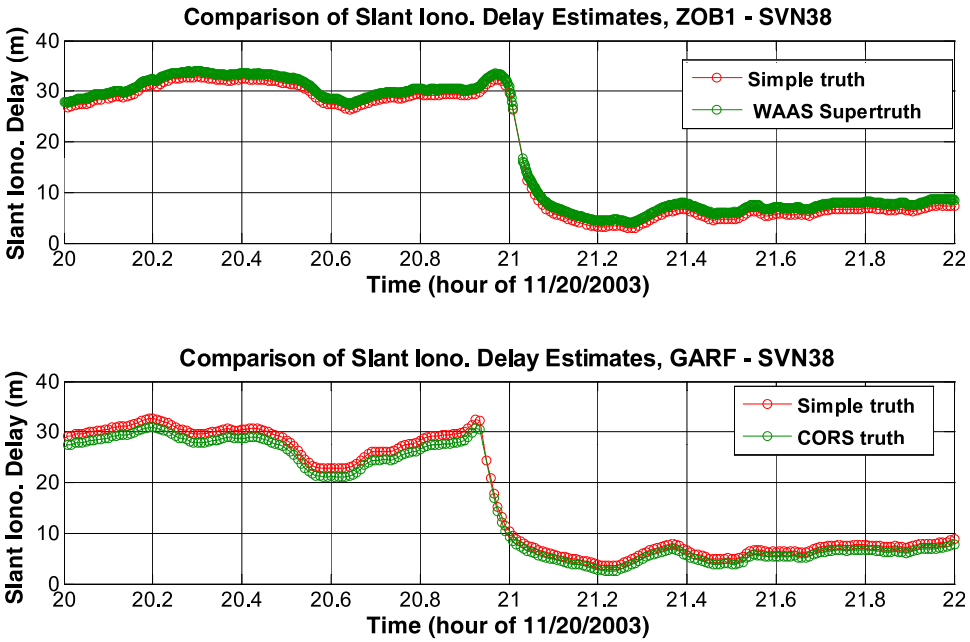

Figure 7. Comparison of dual-frequency slant ionosphere delay estimates, in meters at L1, for ZOB1 and GARF. "Simple Truth" solutions are in red and "Supertruth" solutions are in green.

SVN 38 (PRN 8). The "simple Truth" solutions (red) are compared to the WAAS "Supertruth" (green). The lower plot compares two solutions, the "simple Truth" (red) and JPL post-processed CORS truth (green) for the slant ionospheric delays on L1 measurements between GARF and SVN 38 (PRN 8). For both cases, the two solutions agree well and the discrepancies between two delay estimates are approximately ± 1 m, mainly caused by IFB calibration errors. The ionospheric delay estimation error of 1 m, when divided by the station separation of 51.2 km, is converted to the gradient error of approximately 20 mm/km. In the end, this discrepancy is acceptable because the gradient estimates are accurate enough to identify the most extreme ionospheric anomalies which are a few hundred mm/km.

[45] Figure 8 shows the dual-frequency ionospheric gradients (blue) observed from ZOB1 and GARF viewing SVN 38 (PRN 8) as a function of time. The gradients are calculated by dividing the difference of the "simple Truth" delay estimates by the station separation of 51.2 km. Data outages on dual-frequency estimates are visible especially at the falling edge of the spike in Figure 8, calling into question the reliability of the maximum slope of 387 mm/km at about 68° elevation and 2100 UT. For this reason, manual validation was conducted by comparing the dual-frequency estimates (blue) with the L1 code-minus-carrier estimates of the slope (red). The data outages do not exist in the single-frequency estimates, which are not subject to the relative weakness of L2 semi-codeless tracking loops. Based on the good agreement of the two slope estimates, this event was validated as a real ionospheric anomaly.

[46] The largest ionospheric gradient that has been observed at low elevation (event number 5 in Table 4) is also investigated to examine the performance of the LTIA monitor. Figure 9 compares the dual-frequency-based slope estimates (blue) between WOOS and GARF (which are 74.5 km apart) viewing SVN 26 (PRN 26) with the single-frequency estimates of the slope (red). Again, based on the agreement between the two estimates, the highest slope of 351.7 mm/km that occurred at about 11° elevation was validated. Since the magnitude of this slope estimated from the JPL CORS truth solution was 360 mm/km, the difference on gradient estimates between two solutions is about 8 mm/km in this case. Although small discrepancies between the "simple Truth" and CORS truth solutions exist and are to be expected, it is shown from this case study that the automated procedures

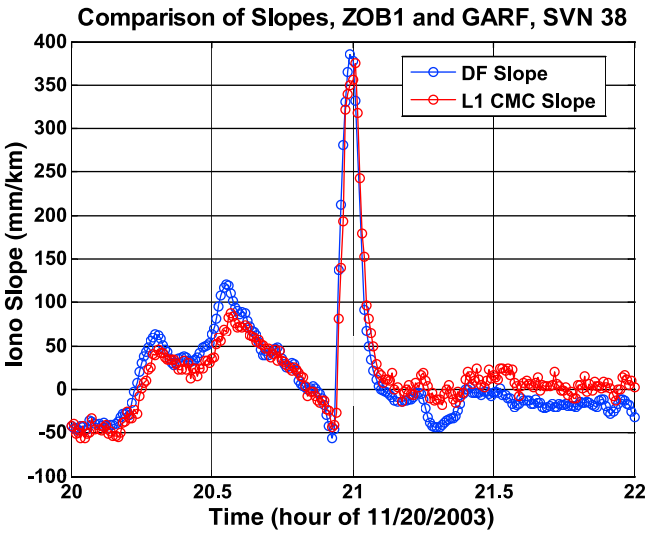

Figure 8. Dual-frequency (blue) and single-frequency (red) estimates of ionospheric spatial gradients between ZOB1 and GARF viewing SVN 38 (PRN 8) at high elevation on 20 November 2003.

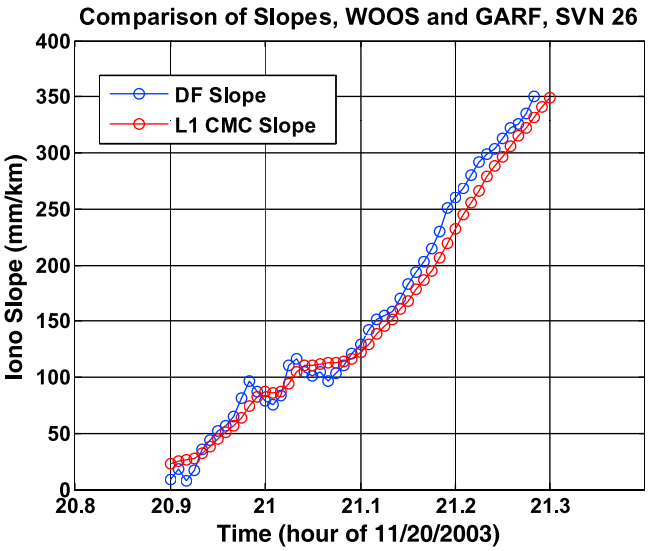

Figure 9. Dual-frequency (blue) and single-frequency (red) estimates of ionospheric spatial gradients between WOOS and GARF viewing SVN 26 (PRN 26) at low elevation on 20 November 2003.

successfully identified the most extreme ionospheric gradients at both high and low elevation, suggesting that "simple Truth" processing is sufficiently accurate.

[47] All of the other anomalies in Table 4 were also validated through this manual validation procedure. For event numbers 10 and 13−16, dual-frequency estimates and single frequency estimates exhibited very similar patterns of ionospheric gradients. However, the two estimates differed considerably in magnitude. The final gradient estimates were determined based on the L1-only estimates, as these form a lower bound on the true gradient [*Datta-Barua et al.*, 2010]. Therefore, for event numbers 14–16, the L1-only estimates are below the monitoring threshold of 300 mm/km.

6.2. Case Study on Nominal Day

[48] This test was conducted on an active but nominal day, 9 November 2004, and the results are summarized in Table 3. The total number of CORS stations in CONUS as of November 2004 was 508. Among those, the number of stations which have other stations within 100 km is 391. Ionospheric gradients were calculated for all possible pairs of 391 CORS stations and all satellites in view. The automated process first searched for any gradients which exceeded 300 mm/km for this test, and it returned 33 candidates. Next, the automated false-alarm screening process successfully eliminated all 33 false candidates. From this case study, we conclude that the LTIA monitor performs as expected also on nominal days (i.e., it did not return any faulty anomaly candidates).

[49] Figure 10 shows the comparison of CORS receiver IFB estimates on 9 November 2004. The mean of differences between the "simple Truth" and JPL CORS truth solutions is very close to zero, and the RMS error is 0.360 ns. This statistics are obtained for the 335 stations for which JPL CORS truth solutions exist, and 100 percent of the differences are within ±2 ns. Note that the underlying assumptions of the "simple Truth" method hold better on less-active days. Thus, as noted above, the improved performance of "simple Truth" bias estimation on 9 November 2004 is not surprising because the ionosphere activity on this date is much less severe than that of 20 November 2003.

7. Conclusions

[50] This paper presents a methodology for long-term ionospheric anomaly monitoring to continuously monitor ionospheric events and check the validity of the current threat model over the life cycle of GBAS. The automation of monitoring procedures is necessary to process vast amount of CORS data (and any data from other sources) at regular intervals and search for ionospheric anomalies more comprehensively. Automated validation procedures are also desirable, but manual validation must be retained because automated results cannot be trusted by themselves. The primary goal of improved automation is further limiting the number of "false" gradients that must be passed on to manual validation.

[51] Simplified truth processing is essential to create ionospheric delay estimates without manual intervention. A simpler and faster algorithm to estimate precise ionospheric delays has been described. One variation of this algorithm has been implemented in the LTIA monitor. The results from two case studies suggest that the quality of "simple Truth" should be sufficient to identify extreme ionospheric anomalies which may challenge the current threat model. However, if the LTIA monitor generates confirmed outputs that exceed the bounds of the current threat model, the generation of improved (offline) truth data may become necessary.

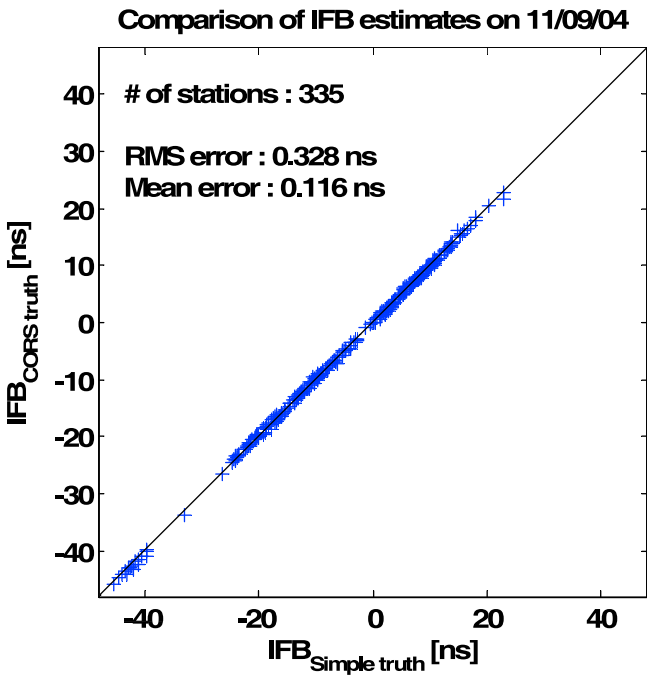

Figure 10. Comparison of CORS receiver IFB estimates on 9 November 2004. "Simple Truth" receiver biases, $IFB_{\_(simple\ truth)}$, are compared to JPL post-processed CORS receiver biases, $IFB_{\_(CORS\ truth)}$.

[52] Once these tools are in permanent operation, they will not only observe and quantify extreme ionosphere events but will also supply broader statistical estimates of nominal and anomalous ionospheric behavior. This will help to understand the statistics surrounding severe events, estimate the probability of occurrence of such events, and more accurately categorize nominal and anomalous ionospheric conditions. This will help us improve GBAS and provide enhanced availability. This knowledge should benefit future GBAS operations, including those different from the "straight-in" CAT I approaches that are now supported. The use of these tools to generate other regional or global GBAS threat models is also expected.

[53] **Acknowledgments.** The authors thank John Warburton of the Federal Aviation Administration (FAA) William J. Hughes Technical Center and his team for their support. We also would like to thank Leo Eldredge, Carlos Rodriguez, Jason Burns, Tom Dehel, Barbara Clark, Hamza Abduselam of the FAA, Oliver Jeannot, Cedric Lewis, Dieter Guenter, and Achanta Raghavendra of the AMT Tetra Tech, Attila Komjathy of the Jet Propulsion Laboratory, and Per Enge, Sam Pullen, Todd Walter, and Juan Blanch of Stanford for their support of this work. The opinions expressed in this paper are solely those of the authors and do not necessarily represent those of the FAA. Sungwook Jung was supported by Basic Science Research Program through the National Research Foundation of Korea (NRF) funded by the Ministry of Education, Science and Technology (2011–0026599).

References

Datta-Barua, S., J. Lee, S. Pullen, M. Luo, A. Ene, D. Qiu, G. Zhang, and P. Enge (2010), Ionospheric threat parameterization for local area global-positioning-system-based aircraft landing system, *J. Aircraft*, *47*(4), 1141–1151, doi:10.2514/1.46719.

Ene, A., D. Qiu, M. Luo, S. Pullen, and P. Enge (2005), A comprehensive ionosphere storm data analysis method to support LAAS threat model development, paper presented at National Technical Meeting, Inst. of Navig., San Diego, Calif.

Hernández-Pajares, M., J. M. Juan, J. Sanz, R. Orus, A. Garcia-Rigo, J. Feltens, A. Komjathy, S. C. Schaer, and A. Krankowski (2009), The IGS VTEC maps: A reliable source of ionospheric information since 1998, *J. Geod.*, *83*(3–4), 263–275, doi:10.1007/s00190-008-0266-1.

Komjathy, A., L. Sparks, and A. J. Mannucci (2004), A new algorithm for generating high precision ionospheric ground-truth measurements for FAA's Wide Area Augmentation System, *JPL Supertruth Doc. 1*, Jet Propul. Lab., Pasadena, Calif.

Komjathy, A., L. Sparks, B. D. Wilson, and A. J. Mannucci (2005), Automated daily processing of more than 1000 ground-based GPS receivers for studying intense ionospheric storms, *Radio Sci.*, *40*, RS6006, doi:10.1029/2005RS003279.

Kou, Y., C.-T. Lu, and D. Chen (2006), Spatial weighted outlier detection, paper presented at SIAM International Conference on Data Mining, Soc. for Ind. and Appl. Math., Bethesda, Md.

Lee, J., S. Pullen, S. Datta-Barua, and P. Enge (2007), Assessment of nominal ionosphere spatial decorrelation for GPS-based aircraft landing systems, *J. Aircraft*, *44*(5), 1662–1669, doi:10.2514/1.28199.

Lee, J., S. Datta-Barua, G. Zhang, S. Pullen, and P. Enge (2011a), Observations of low-elevation ionospheric anomalies for ground-based augmentation of GNSS, *Radio Sci.*, *46*, RS6005, doi:10.1029/2011RS004776.

Lee, J., J. Seo, Y. S. Park, S. Pullen, and P. Enge (2011b), Ionospheric threat mitigation by geometry screening in ground-based augmentation systems, *J. Aircraft*, *48*(4), 1422–1433, doi:10.2514/1.C031309.

Ma, G., and T. Maruyama (2003), Derivation of TEC and estimation of instrumental biases from GEONET in Japan, *Ann. Geophys.*, *21*, 2083–2093, doi:10.5194/angeo-21-2083-2003.

Menvielle, M., and A. Berthelier (1991), The *K*-derived planetary indices: Description and availability, *Rev. Geophys.*, *29*(3), 415–432, doi:10.1029/91RG00994.

Pullen, S., Y. S. Park, and P. Enge (2009), Impact and mitigation of ionospheric anomalies on ground-based augmentation of GNSS, *Radio Sci.*, *44*, RS0A21, doi:10.1029/2008RS004084.

Radio Technical Commission for Aeronautics (RTCA) (2004), Minimum aviation system performance standards for Local Area Augmentation System (LAAS), *Rep. DO-245A*, Washington, D. C.

Seo, J., J. Lee, S. Pullen, P. Enge, and S. Close (2012), Targeted parameter inflation within ground-based augmentation systems to minimize anomalous ionospheric impact, *J. Aircraft*, *49*(2), 587–599, doi:10.2514/1.C031601.

Sugiura, M., and T. Kamei (1991), Equatorial Dst index 1957–1986, *IAGA Bull.*, *40*, 7–14.